Journal of Materials Chemistry C

Accepted Manuscript

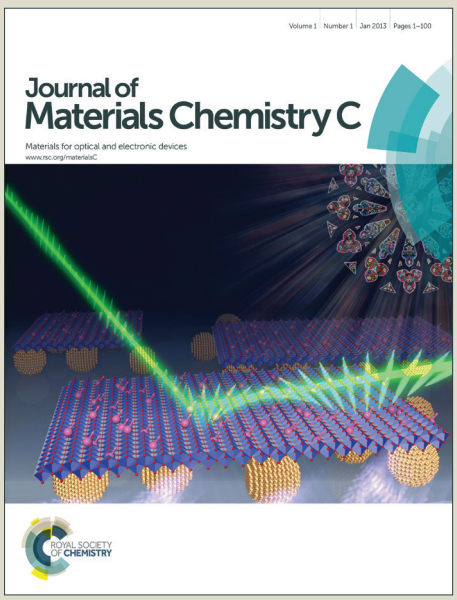

ROYAL SOCIETY OF CHEMISTRY

www.rsc.org/materialsC

Eu^{3+} activated $CaGa_2O_4$ wide band gap (WBG) material for solar blind UV converter: Fluorescence and photo-conductivity performance†

M. Rai[a], S.K. Singh[b,*], K. Mishra[a], R Shankar[c], R.K. Srivastava[c], S.B. Rai[a]

[a]Department of Physics, Banaras Hindu University, Varanasi-221005, INDIA

[b]Department of Physics, Indian Institute of Technology (Banaras Hindu University), Varanasi-221005, INDIA

[c] Department of Electronics and Communication, J. K. Institute of Applied Physics and Technology, University of Allahabad, Allahabad- 211002, INDIA

---

[*]**Corresponding author**

E-mail address: *sunilcfsl@gmail.com, sunilks.app@itbhu.ac.in (S. K. Singh)*

Tel.: *+91-8574027822,* ***Fax:*** *+91 542 2369889*

† Electronic supplementary information (ESI) available: Fourier transform infrared and Raman spectrum of Na^+, Eu^{3+} co-doped $CaGa_2O_4$ (Fig. S1)

Abstract

Herein, we have probed a wide band gap material, $CaGa_2O_4$ co-doped with Eu^{3+}/Na^+, which is fairly transparent (≥95%) in visible region and efficiently absorbs solar blind UV radiation. Importantly, the absorbed UV energy can be realized both in terms of fluorescence and photoconductivity as well. X-ray diffraction studies confirms that, $CaGa_2O_4$ exhibits two orthorhombic polymorphs $CaO.Ga_2O_3$ I (major) and $CaO.Ga_2O_3$ II (minor). Vibrational spectroscopy establishes the first quantitative insight into the phonon frequency of the material. Host itself gives UV-blue and red emission driven by host: band to band and trap level transitions, respectively, under UV excitation. A substantial overlap between emission spectrum of the host and excitation spectrum of Eu^{3+}; decrease in emission intensity and decay time (8.82 μs from 9.2 μs) of the host emission, after Eu^{3+} doping; and evolution of a short rise-time (~10 μs) in decay curve of Eu^{3+} reveal that, the host efficiently transfers its energy to Eu^{3+} ion. Co-doping of Na^+ further enhances the emission intensity (~7 times), decay time and rise-time of Eu^{3+} emission. Likewise the intrinsic behavior of Ga_2O_3, this material also shows significant transient photoconductivity under UV illumination, photocurrent is of the order of μA, but with slow time constant ~40 min. Thus, excellent optical properties prove superiority over photoconductivity for UV-to-visible converter application. Such WBG optical materials can be coupled to silicon-based commercial detectors for their wide use in areas ranging from invisible flame sensing to UV astronomy, etc.

Key Words: Gallate, lanthanide, wide band gap material, fluorescence, photoconductivity

1. Introduction

Ultraviolet (UV) light sensing, particularly development of materials for *solar-blind* UV detection, has emerged as an important area of research due to its potential applications in many different fields viz. astronomy/solar and space physics, flame sensing, chemical and biological analysis, optical communication, civil and military applications, etc. [1-4]. In principle, when it comes to UV light detection, complete UV spectral range is divided into four spectral components; UV A (400-320 nm), UV B (320-280 nm), UV C (280-200) and far UV (200-10 nm). The components UV C and far UV are termed *solar-blind*, as the Sun's radiation at these bands do not reach earth's atmosphere [5]. The principle mechanism involved for the *solar-blind* UV detection relies on the measurement of transient photoconductivity and/or fluorescence. Therefore, several architectures based on different exotic host matrices e.g. organic, inorganic, hybrids, nanostructures, thin films etc. have been explored widely for the purpose, and some of them are attaining commercial viability too [6-16]. However, the material stability, especially in terms of luminescence, which is a key limitation with the organics and thin films; the ecological viability, some materials are very toxic (like fluorides) and not biodegradable; and the cost effectiveness still imposes a strong quest for the search of exotic low cost efficient alternative materials for solar blind UV sensing applications.

Looking into more detail, wide band gap (WGP) materials (band gap above ≈ 3.1 eV, 400 nm) are highly preferred for UV light sensing applications. The wide band gap on one hand allows good optical transparency, which makes them insensitive towards visible-infrared (IR) radiation with minimal background, and on the other hand offers excellent photo-response in UV spectral range. The underlying physics behind their sensitivity to UV illumination is mainly explained in terms of defect level induced phenomenon. Such oxides with a fundamental

bandgap >3.1 eV are insulators at room temperature in the undoped state [17]. By suitable doping (cationic or anionic), or by creating non-stoichiometry via introducing oxygen deficit defect states, lattice point defects are introduced close to the conduction (donor level) and valence (acceptor level) bands. These defect levels act as trap centre for excited electrons, and have a very low threshold temperature (~kT) at which they can release electrons into the conduction band providing semiconducting behavior (delocalized property-conductivity); or on the other hand, they can recombine radiatively with the hole in the acceptor level giving broad intermediate band emission usually in visible region (localized property-fluorescence), also called donor acceptor pair (DAP) recombination process. Both these properties (localized and de-localized) are complementary to each other and hardly co-exist evenly in any material.

Paradoxically, gallium oxide, β-Ga_2O_3, is known to exhibit both the properties and can be useful to sense UV light both by conductivity and fluorescence methods [18]. In this light, gallium based double oxides (gallates) are a brilliant class of optically rich material under UV illumination, e.g. gallate of yttrium, gadolinium, lithium, zinc, copper, lanthanum, etc have been widely explored both for photoconductivity and/or fluorescence based applications [19-23]. However, calcium gallium oxide ($CaGa_2O_4$, CGO), a member of this series, has been long overlooked in spite of its excellent optical transparency (in visible region), high photo-stability, and economic availability, etc [17-21]. Our idea is to explore the possibility of the CGO host as UV-visible light converter, particularly for *solar blind* UV spectral range, by fluorescence measurements. Further idea is to transfer the excited energy of both the trap level and conduction band to an activator (lanthanide) ion, which can release this energy in terms of fluorescence (electronic transitions). Of course, the transient photoconductivity measurement has also been performed to complete the study. No work to the best of our knowledge has ever tackled the task

of investigating the solar blind UV to visible converter application in gallium based WBG material by the energy transfer from trap levels/conduction band to lanthanide ions and fluorescence thereof.

For this purpose, we have synthesized both pure CGO and Eu^{3+} doped CGO samples by using conventional solid state reaction method. Eu^{3+} has been doped in the material as it is well known for its highest fluorescence quantum efficiency among other lanthanides, reported so far, under UV exposure. It gives sharp emission line at ~ 613 nm, which gives a perception of a saturated red color tone, quite useful for sensing purposes. Moreover, in this host-activator combination, in principle, the Eu^{3+} can be excited by many different ways, viz. by exciting host absorption band (conduction band) and associated trap (defect) levels, by charge transfer state of Eu^{3+}, and also by exciting the characteristic f-f transitions of Eu^{3+} ions, which all together covers entire UV range, including *solar blind* region. Further, In CGO host, since, Eu^{3+} ions replaces Ca^{2+} site, following the Shanon ionic radii rule [24]; therefore, this replacement of divalent Ca ion by trivalent Eu ion creates the charge imbalance, which has been compensated by co-doping of Na^{+} ions. Detailed structural, optical transparency, steady state (excitation, emission) and time domain fluorescence of the host and doped lanthanide ion, color chromaticity coordinate, and photo-conductivity measurements, etc. have been performed in detail and analyzed.

2.0 Experimental

2.1 Materials and Method

The samples were prepared by conventional solid state reaction method. $CaCO_3$, Na_2CO_3 Ga_2O_3, Eu_2O_3 (Alfa Aesar, 99.99 %) were used as the starting material. The stoichiometric ratio of these compounds was thoroughly mixed, with few drop of acetone, in an agate mortar and the mixture

was pelletized into disc of 10 mm diameter and 0.5 mm thickness. The pellet was calcined at 900 ^{o}C for 4 h, and then sintered at 1250 ^{o}C for 6 h. This temperature was chosen in order to avoid the possibility of melting ($CaO\text{-}Ga_2O_3$ melts congruently at 1369 ^{o}C). The material was optimized for 1 mol% Eu^{3+} doping and then doped with *x* mol% Na^{+} (*x* = 0 to 8, in steps of 2).

2.2 Characterization

For structural characterization, X-ray diffraction (XRD) patterns were recorded using an 18 kW Cu rotating anode based high resolution Rigaku X-ray powder diffractometer fitted with a curved crystal monochromator in the diffracted beam. Fourier transform infrared (FTIR) measurement was carried out on Spectrum 65 spectrophotometer, Perkin Elmer and the spectra were collected at a resolution of 2 cm^{-1}. Raman spectrum was recorded using 514.5 nm line of Ar^{+} laser on a micro-Raman setup (Renishaw, UK) equipped with 2400 lines/mm grating and a peltier cooled CCD (charge coupled detector). The *GRAM-32* software was used for data collection. Spectrometer is assisted with an Olympus (Model: MX50 A/T) microscope to focus the laser light on to the sample and to collect the scattered light at 180^{0} geometry. UV-visible absorption spectrum was carried out using Shimadzu UV-2600 UV-Vis spectrophotometer (model A116650). The spectrum was recorded in reflectance mode and scanned twice to remove any background peaks.

Photoluminescence excitation (PLE) and emission (PL) measurements were performed using a Fluorolog-3 spectrofluorometer (Model: FL3-11, Horiba Jobin Yvon) equipped with 450 W Xenon flash lamp. The lifetime measurements were performed using pulsed Xenon lamp (25 W) by the same setup. The entire spectrum is recorded after lamp intensity correction and spectral correction for PMT (photomultiplier tube) and for the slit width fixed at 2 nm. For the

fluorescence measurement under laser excitation, the fourth harmonic (266 nm) of Nd:YAG laser (pulse width 4 ns, Litron nano TRL) was used and spectrum was recorded using optical fiber attached to CCD (Ocean Optics QE65000). For photoconductivity and dark-conductivity measurements, a cell constituting the sample pellet, sandwiched between Cu electrodes etched on a Cu plate printed circuit board, is mounted in a dark chamber with a narrow slit through which the sample is illuminated. The direction of illumination is normal to the field across the electrodes. To measure the UV-Vis photo-response, the cell is initially kept in dark till it attained equilibrium. A 300 W mercury lamp is used as photo-excitation source and current is measured using RISH Multi 15S with adapter RISH Multi SI 232. The digital image of the sample is taken by exposing the samples with a 6 W UV lamp (GeNei, France).

3.0 Results and discussions

3.1 Structural characterization: XRD, FTIR and Raman measurements

The typical X-ray diffraction patterns of pure host of CGO, Eu^{3+}: CGO and Na^{+}, Eu^{3+} co-doped CGO are shown in Fig.1. The pure host forms a dominant phase of orthorhombic CGO (JCPDS 016-0593) with some peaks arising due to another orthorhombic CGO (secondary phase) phase (JCPDS 014-0251). The polymorphic structure of $CaO.Ga_2O_3$ has been earlier studied by Jeevaratan and Glasser [24]. They have also found two orthorhombic polymorphs secondary phase (minor). With Eu^{3+} doping, these peaks due to secondary phase are suppressed. However, co-doping of Na^{+} (4 mol %) in Eu^{3+}: CGO do not show any further change in structure e.g. phase, except a small peak shift towards lower 2θ (~ 0.0384^{o}) side. Evolution of a minor secondary phase is due to the presence of polymorphs of $CaO.Ga_2O_3$ in the crystal structure [24]. $CaO.Ga_2O_3$ exhibits two orthorhombic polymorphs $CaO.Ga_2O_3$ I and $CaO.Ga_2O_3$ II along with a

monoclinic m-$CaO.Ga_2O_3$. The m-$CaO.Ga_2O_3$ is a metastable form under all cases and inverts to $CaO.Ga_2O_3$ I polymorphic form. However, polymorphic forms I and II both do not have separate field of stability, and so the phase equilibrium between them remains uncertain [25]. The stoichiometry with precise 1:1 molar ratio develops the polymorphic form-I, however, even a slight deviation in this ratio yields the polymorphic form-II, in addition.

Doping with Eu^{3+} ion (~1.066 Å) is expected to replace Ca^{2+} site (~1.00 Å), as the ionic radius of Ga^{3+} (0.62 Å) is very small, resulting in overall reduction of CaO in the matrix. This reduction in CaO helps to retain the 1:1 ratio, and so diffraction peaks corresponding to polymorphic form-II is significantly reduced resulting in single phase CGO with lattice parameters a = 7.73, b = 9.14, c = 10.36 A, V = 731.96 A^3, $Pna2_1$ (C_{2v}) space group. A small peak shift towards lower 2θ side, upon Na^+ co-doping in Eu^{3+}: CGO, can be understood on the basis of the crystal structure. The AB_2O_4 type compounds usually form *stuffed tridymite* structures with an open framework of BO_4 tetrahedra and A^{2+} ions stuffed within the holes in the framework [26]. But, due to significantly smaller ionic radii of Ca^{2+}, the structure of CGO is a distorted stuffed *tridymite*. The ionic radius of Na^+ (~1.02 Å) is smaller than Eu^{3+}, therefore, when it replaces some Ca^{2+} site the cell volume is reduced a little bit. This increases the d spacing and hence peaks shift towards lower 2θ side. Of course, since the stuffing area available is a hole large enough, there is no change in structure or phase of the crystal upon additional doping (upto an extent).

Further to confirm the presence of CGO phases and also to have an idea about the phonon frequency of the host matrix, FTIR and Raman spectroscopy techniques have been used. Fig S1 shows the FTIR and Raman spectra of Na^+, Eu^{3+} co-doped CGO phosphor. The fundamental vibrational bands in CGO host arise due to the stretching and bending of tetrahedra or octahedra

structural units. The IR bands lie in the region 490-800 cm^{-1} with two prominent absorption peaks at 529 cm^{-1}, associated with the Ga–O–Ga bridges between GaO_4 tetrahedra, and at 586 cm^{-1}, ascribed to superposition of Ga–O–Ga vibration. A sharp absorption peak at 1382 cm^{-1} is due to stretching vibration of NO (ν_{NO}) confirming the presence of nitrogen also, which may have been adsorbed from the atmosphere during high temperature synthesis. The broad peaks at 1460 and 1635 cm^{-1} are mainly due to O-H vibrations which arise due to some moisture content in the sample. Raman spectrum also shows the presence of intense peak at 538 and 590 cm^{-1}, similar to IR absorption spectrum, along with weak bands. All the indexed peaks match well with the reported assignment of the IR and Raman bands for $CaGa_2O_4$ [27]. Thus, the vibrational analysis also supports the formation of CGO phase. Also, the analysis confirms the phonon frequency of the host material lies in the range 500-600 cm^{-1}.

3.2 Optical absorption and optical band gap measurement

The UV-visible absorption spectrum of CGO host is shown in Fig. 2. Figure reveals that there is strong absorption below 330 nm i.e. material has strong tendency to absorb UV photons (particularly UV-B and UV-C) and it reduces drastically for visible region. The large absorption coefficient for UV light is a characteristic of band to band transition. Near to 400 nm, although relatively weak, there is a small absorption peak followed by a hump like structure. Appearance of this peak signifies an onset of inter-band absorption which may arise due to the formation of defect levels into the energy band gap. Since the defects or traps formed and the transition in between them is always phonon assisted phenomenon, it gives a very broad absorption band, as is clear from the spectrum also; the absorption tail extends upto nearly 530 nm. The transmittance is a direct consequence of absorption data. Therefore, herein, up to ~400 nm the

transmittance is very poor due to host absorption. While, for the 400- 550 nm region, it is more than 60% transparent and rest of the energy is fed to the system. Lastly, after the 550 nm region, transmittance increases rapidly and approaches to almost 100% for the rest of the visible-IR spectrum. Conclusively, CGO has strong UV absorption and visible transmittance. Based on the absorption data, the optical band gap has been also calculated using Wood and Tauc model according to which the absorbance (α) and optical band gap are related as-

$$h\nu\alpha \sim (h\nu - E_g^{opt})^{\gamma} \quad (1)$$

where, γ=1/2 for direct allowed, and γ=2 for indirect allowed transition [28]. A plot to measure band gap energy is shown in the inset of Fig. 2. By extrapolating the $(\alpha h\nu)^2$ curve we get the direct optical band gap at 3.6 eV (344 nm). Whereas $(\alpha h\nu)^{1/2}$ curve gives indirect band gap at 3.1 eV (400 nm). This indirect band gap is the sub band gap that arises due to the formation of a donor level below the conduction band at a separation of ~0.5 eV. Thus, CGO is an indirect band gap semiconductor.

3.3 Steady state fluorescence measurement

3.3.1 PLE and PL measurement of the host $CaGa_2O_4$

The photoluminescence excitation (PLE) spectrum of CGO corresponding to emission at 435 nm is shown in Fig. 3(a). There is two distinct excitation region-one is the dominant band from 230 - 280 nm peaking at 255 nm, ascribed to the band to band transition, followed by another relatively weaker broad band from 300-400 nm, with maxima at 375 nm, which has been assigned due to the defect level excitation. Point defects like ionic vacancy, indistinct grain boundaries, etc are very common and well reported in Ga based wide band gap materials [29,30]; and in addition to this, nitrogen adsorption from the air during the high temperature synthesis,

moisture absorption, etc. also increases the load of defects. Such defects are reluctantly introduced in the lattice during synthesis, and are directly responsible for the intermediate band transitions, which are controlled by various recombination processes. Based on the PLE spectrum, the PL is monitored at two selective excitation wavelengths i.e. 255 nm and 375 nm. Fig. 3(b) shows the PL of CGO host at λ_{exc} = 255 nm. There is a broad band bluish white emission ranging from 300-800 nm at a significant Stokes shift of ~195 nm. This indicates a strong electron phonon coupling and localization of recombining charges [31]. In order to understand this Stokes shifted band emission we need to elucidate its origin. A vacant atomic site or a vacancy (V) is a common type of lattice point defect introduced into the host during synthesis. Due to this, oppositely charged ions are introduced resulting in Ga-O vacancy pair $(V_O,V_{Ga})'$ in Kröger-Vink notation [32]. Similar could be the case with Ca also resulting in Ca^{2+} vacancy. When any defect is introduced in the crystal it breaks the periodical arrangement of the lattice allowing the formation of localized states (trap levels) in the forbidden band gap. These localized states are nothing but the charged states of donor trap (negatively charged V_O) and acceptor trap (positively charged V_{Ga} or V_{Ca}). These types of oxygen vacancies (defect) are generally shallow donors (~meV) and their position below the conduction-band edge depends on the effective mass m_e^* and dielectric constant ε of the medium [33]. Due to this small energy difference between donor level and conduction band, these levels are ultimately populated upon excitation through non-radiative relaxation. Thus the recombination of electron and hole from these donor acceptor pair (DAP) defect states results in blue intermediate band emission. It is worth noting here that, the ionization energies of these donors and acceptors are of the order of k_BT only and hence at room or elevated temperature they may contribute to the conductivity also, which has been discussed in detail in the photoconductivity section.

However, under laser excitation by 266 nm, we obtain a structured emission spectrum as shown in Fig. 3(c). A UV-Vis broad emission ranging from 300-650 nm appears (similar to Fig. 3(b)) followed by a prominent band in red–NIR region, from 650-850 nm. The origin of this red emission is attributed to the presence of nitrogen impurities. Earlier, FTIR study has already confirmed the existence of nitrogen. Vanithakumari et. al. have also reported similar red luminescence in Ga_2O_3 from the unintentional doping of the nitrogen which generates deep acceptor levels in the mid of the band gap [29]. The existence of the structured NIR emission becomes more evident when we directly probe the donor trap defect level by exciting with 375 nm as shown in Fig. 3(d). Thus on the basis of all these information, emission mechanism in $CaGa_2O_4$ is elucidated by the energy band diagram shown in the left part of Fig. 4.

The first part of the figure reveals the possible position of the trap levels and different channels of recombination. Under 255 nm band to band excitation, the donor and acceptor trap are also populated due to their shallow depth. Now, the possible four modes of emission are as follows: 1 is the donor to acceptor trap (DAP) recombination, 2 is the electron de-trapping from donor to valence band, 3 is the conduction band to acceptor trap recombination and 4 is the band to band emission in UV range. Thus host itself emits in UV-blue region. The deep nitrogen trap also acts as recombination centre for the donor trap giving red emission. Due to the admixing of all these channels under 255 nm we observe a broad feature of emission from UV to NIR region. However, under direct defect level excitation, the UV emission disappears and only the bands from donor trap appear with significant emission in blue and red region. Thus by this way, through the involvement of defect level, wavelength dependent color tunable emission is observed. This dependence is only observed under low intensity incoherent excitation by Xe lamp, but, under laser excitation, all the emission bands appear simultaneously as shown in Fig.

3(c). The intense laser beam is sufficient enough to stimulate all the recombination processes between different induced defect levels.

Excellent emission of the host in UV-blue region opens the possibility of sensitizing (energy transfer) to different rare-earth ions; particularly Eu^{3+}, as the strongest excitation of this rare-earth ion (both charge transfer band and f-f transition) is well known to lie in the range of observed emission spectrum of the host. Thus, in this way the Eu^{3+} co-doped CGO has fair potential to be used as solar blind UV to visible converter; to establish this conjecture, optical properties, including steady state and time domain fluorescence, have been explored in detail in the next section.

3.3.2 PLE and PL measurement of Na^{+}, Eu^{3+} co-doped $CaGa_2O_4$

Figure 5(a) shows the excitation spectrum of Eu^{3+} doped and Eu^{3+}, Na^{+} co-doped CGO monitored for $^5D_0 \rightarrow {}^7F_2$ transition of Eu^{3+}. The spectra consist of a broad band from 240–310 nm along with sharp peaks in the range of 360-580 nm. These sharp peaks are the excitation energies of Eu^{3+} ions corresponding to the electronic transitions of the 4f- electron manifolds [34]. These are the allowed spin-flip transitions from $^7F_0$ to various excited levels (mainly ^5D_J). The most intense peak is indexed to the $^7F_0 \rightarrow {}^5L_6$ excitation at 391 nm. The broad band region is due to the host absorption band and common ligand to metal charge transfer (LMCT) mechanism-termed as Eu-O charge transfer band (CTB). It is difficult to distinguish both the band separately. However, multiple peaks fit analysis clearly shows that the broad band structure contains two peaks, identified with their maxima at 255 nm and 278 nm, and can be assigned to the host absorption and CTB, respectively. Eu^{3+} has strong affinity for one electron to be stable and this makes significant integration of its f-orbitals with the oxygen p-orbitals of the host

lattice. Due to the involvement of host the nature of CTB is broad. These CTBs are generally excited at high energy (250-300 nm) and at such a high energy these transitions may include an electron transfer from $O^{2-} \rightarrow Eu^{3+}$ or from Eu^{3+} to the conduction band [35]. However, latter is less probable due to the unstable nature of Eu^{4+}. Excitation spectrum of the Na^{+} co-doped sample significantly shows an intensity enhancement in the excitation bands/peaks. Although, there is no change in the peak position of Eu^{3+} levels, yet, a slight shifting of CTB is observed towards higher wavelength. This red shift signifies the formation of CTB at energy lower than that as in the case of Na^{+} un-doped sample. This is expected due to the synergetic effect of Na^{+} ion. It is already well reported that alkali ions like Na^{+}, Li^{+}, K^{+} not only act as charge compensator, but they also affects the crystal structure to some extent including a change in crystallinity, particle size, surface morphology, etc. [36].

Figure 5(b) shows the effect of Na^{+} co-doping on the emission spectrum of Eu^{3+}: CGO under the 255 nm excitation. Here, Na^{+} (ionic radius ~1.02 Å) is used due to its matching ionic radii with Ca^{2+} ions (ionic radius ~1.0 Å). Inset shows a variation in the emission intensity (for the transition at 613 nm) which initially increases with Na^{+} concentration with a maximum at 4 mol% (a maximum of about ~7 times enhancement in the Eu^{3+} emission is attained), beyond which it starts decreasing mainly due to the concentration quenching effect. It is mainly due to the fact that at higher concentration of Na^{+}, a local distortion is produced around Eu^{3+} ions and hinders its direct activation due to over population. Likewise the excitation spectrum, emission spectrum also shows two distinct regions; an almost flat region ranging from 280 to 480 nm corresponding to highly suppressed defect emission, and the characteristic emission peaks of Eu^{3+} from $^5D_0$ to various ^7F_j levels. The maximum emission intensity is observed at 613 nm arising due to $^5D_0 \rightarrow {}^7F_2$ transition. As clearly observed, a significant reduction in the host

emission as compared to pure host implies a fair probability of energy transfer from host to the Eu^{3+} ions, as the prominent excitation wavelengths of Eu^{3+} (361, 381,391,413, 463, and at 526 nm) overlaps to the broad band emission (in the range of 300-600 nm) of the host. The charge transfer band is the immediate result of band to band excitation by 255 nm. Since the band is formed for a very short time scale just below or adjacent to the CB, the population from it is soon relaxed to Eu^{3+} levels beneath it and the non radiative channels surpass various intra bands and finally populate the metastable $^5D_0$ level from where different peaks in red region are observed.

Figure 5(c) shows the CIE (international commission on illumination) coordinate of various emissions at the 255 nm excitation, and the digital photograph of the pellet under 254 and 365 nm UV lamp exposure. The CIE coordinate of CGO at (0.24, 0.29) lies in the bluish white region in agreement to the visibility in the digital photograph. However, after Eu^{3+} doping, sample beautifully glows with red emission under 254 nm UV lamp exposure; and the CIE for the corresponding sample lie at (0.62, 0.38). After Na^+ co-doping, the CIE coordinate of the red emission shifts to (0.64, 0.36); i.e. Na^+ not only enhances the emission intensity but also improves the color perception. Hence, Na^+ co-doped sample could be seen more intense than undoped one. Under the 365 nm lamp exposure, the whole image gives violet background and due to the admixing of red and violet the overall perception of the Eu^{3+} doped pellet is of pinkish tinge.

Further, the emission of Eu^{3+} have been measured by exciting the sample by different excitation wavelength, 255, 278 and 391 nm, certainly to probe the emission from different mechanism (see Fig. 5(d)). Considering Eu^{3+}: CGO first, the 255 nm corresponds to the host absorption (conduction band) and the excited energy is migrated to the donor trap level, through tunneling, also. Herein, although Eu^{3+} has no direct excitation, yet, from the CTB and through

the involvement of energy transfer process Eu^{3+} is excited. Thus the emission spectrum consists of the bands due to host as well as of Eu^{3+} both. As we move to the longer excitation wavelength, i.e. 278 nm, CTB is resonantly excited and hence Eu^{3+} emission appears with enhanced intensity along with the emission of host also. Most intense is the emission through 391 nm excitation, since we are direct probing the $^5L_6$ level. This results in direct intense Eu^{3+} emission with least host contribution. This variation in the emission intensity is well in agreement with the excitation spectrum. The trend, however, reverses in the Na^+ co-doped samples. Emission under 278 and 255 nm excitation is somewhat similar to that we observed in the case of undoped Na^+. However, interestingly, the emission from 391 nm is the weakest one here in spite of the best excitation at this wavelength (see excitation spectrum). The exact reason behind this was not very clear; but it is expected that, the variation related to the excitation wavelength may be due to the interaction among Eu^{3+} neighbors (O, Na and Ga tetrahedra) and incident light [34].

One additional points of attention is the reduction in FWHM (full width at half maximum), which is obvious as transitions become sharp due to matrix symmetrization. The $^5D_0 \rightarrow {}^7F_1$ is a magnetic dipole transition and intensity of this transition is independent of the surrounding environment. Hence, it can be used as a reference for the site symmetry. On the contrary, the absorption band $^7F_0 \rightarrow {}^5D_2$ and emission band $^5D_0 \rightarrow {}^7F_2$ are hypersensitive transitions. Intensity of the electric dipole transition $^5D_0 \rightarrow {}^7F_2$ does not appear if it is at site with centre of symmetry. Its intensity increases as the asymmetry increases. Thus, the ratio $(^5D_0 \rightarrow {}^7F_2)/(^5D_0 \rightarrow {}^7F_1)$ is regarded as asymmetry ratio to monitor the rare-earth site symmetry and is given as [37]:

$$A = \frac{\int_{600}^{680} I_2 \, .d\lambda}{\int_{575}^{600} I_1 \, .d\lambda} \qquad (2)$$

where, 2 and 1 refers to the transitions for j= 2 and 1. A_{21} increases in the Na^+ co-doped sample for all three excitations i.e. 1.62 to 2.82 for λ_{exc} 255 nm, 1.50 to 2.71 for λ_{exc} 278 nm, and 1.85 to

1.91 for λ_{exc} 391 nm. This clearly reveals an increase in the asymmetric environment around Eu^{3+} created by the Na^{+} presence and hence in the intensity of electric dipole transition.

3.4 Time resolved photoluminescence (TRPL) measurement: Energy transfer studies

The partial energy level diagram showing the mechanism of emission in Eu^{3+} is shown in the right part of Fig. 4. This mechanism is based on the fact of an energy transfer from the host to the activator Eu^{3+} ion. To establish this, a detailed time domain fluorescence measurement was carried out for the emission of host and Eu^{3+} ions as well. The decay profile of the emission of the host (435 nm) and rare earth ion (613 nm) is shown in Fig. 6. Pure host has the life time of ~9.2 μs which is characteristic of 435 nm blue emission (t > 1 μs). The decay is not perfectly exponential (fitting parameter = 0.98) suggesting only partial involvement of transition probability of the defect levels. Rather, a complex kinetics is involved which is influenced by the competitive recombination of other channels (as shown in Fig. 4). Both the results are in agreement to the one reported by Binet et al. [18]. However, when Eu^{3+} is doped in CGO, the decay time of the host emission reduces to ~ 8.82 μs. This is the direct consequence of potential energy transfer from host to the Eu^{3+} activator ions. It is obvious as the broad band blue emission of the host overlaps with the sharp excitation bands of Eu^{3+}. Further, with Na^{+} co-doping, lifetime again increases and reaches to ~9.13 μs i.e. approaches to the case of pure host. This is the case of system stabilization. Na^{+} is well known for the matrix symmetrization and enhancing crystal growth and as a result brings the system to structural stability. This increases the life time of the emitting levels (here recombination centers) and enhances the overall emission.

Figure 6(b) shows the decay kinetics of Eu^{3+} red emission (613 nm, $^5D_0 \rightarrow {}^7F_2$ transition) under 255 nm excitation wavelength. The life time of the $^5D_0$ level increases from 1.232 ms to

1.305 ms for Na^+ co-doped sample compared to undoped Na^+ sample due to similar reason as in the case of pure host. All the life time is obtained by mono exponential decay fitting. Along with the decay time, a small rise time (10 μs) is also observed in the case of doped CGO, inset in Fig. 6(b), which is further enhanced (30 μs) after Na^+ co-doping. This increase in rise time suggests that more energy is fed to the Eu^{3+} levels from upper CTB or host emission i.e. energy transfer from host to guest becomes favorable in the presence of Na^+ ions.

3.5 Transient photoconductivity measurement

Till now, we have explored the photo-response of CGO against UV photons and found that it is a transparent oxide with radiant luminescence properties. The photoconductivity measurement further explains the probability of charge carrier generation and recombination in the material and hence interprets the material quality for efficient UV detection. The UV photoconductive response curve for the CGO and Eu^{3+}, Na^+ co-doped CGO is shown in Fig. 7. Initially, the dark current is of the order of ~ 400 pA and is almost constant throughout the range of measurement. Under fixed bias voltage of 20 V, the curve for Eu^{3+}:CGO shows a slow and steady rise under illumination and then decays exponentially after the lamp is turned off. The observed photocurrent results from the carrier excitation due to light absorption (UV photons) of energy greater than the band gap. Initially a trough is evolved after ON stage and continues to persist up to 700 s. This decrease in photocurrent even under steady illumination may arise due to the adsorbed O_2 molecules on the surface. However, after 700 s, there is continuous increase in the current which attains saturation at 0.03 μA, i.e. there is significant rise of ~100 times compared to the magnitude of dark current.

Under UV photons this current is attributed to the generation of electron-hole pairs from valence-conduction band or acceptor trap-conduction band as shown in the inset of Fig. 7. Noticeably, here is a long time constant corresponding to the rise time which depends on the rate of charge generation as well as charge recombination and hole trapping. The photo-generated charge carriers may recombine or fill the trap levels. When they fill these trap states they are no more available for conduction, instead charges build up in these traps resulting in a situation of *chemical capacitance*. Under both conditions conductivity slows down. These O^{2-} vacant materials are primarily n-type and Fermi level lie close to CB. Therefore, donor traps are always filled with electrons even under dark. So, the photoconductive behavior is mainly preceded by the holes trapped/captured in the acceptor level. Thus, this hole trapping/detrapping also gives rise to the slow photoconductive response. The photoconductivity can be represented in terms of following rate equation for the change in concentration of conduction band electrons, valence band holes and trapped holes [38]:

Rate of change of electrons in CB: $\frac{dn}{dt} = W_{gen} + \Phi\sigma_h\left(D_{total} - D_{filled}\right) - h.W_{rec}$ (3)

Rate of change of holes in VB: $\frac{dh}{dt} = W_{gen} + MB\ factor - h.W_{rec} - h.W_{cap}$ (4)

Rate of hole de-trapping: $\frac{dD_{filled}}{dt} = \Phi\sigma_h\left(D_{total} - D_{filled}\right) + h.W_{cap} - MB\ factor$ (5)

where n, h are the number of free electrons and holes; W_{gen}, W_{rec} and W_{cap} are the rate of photo-generation, recombination and hole capture by the acceptor trap respectively; Φ is incident photon flux and σ_h is capture cross section; D_{total} and D_{filled} are the total trap density of the holes and filled trap density respectively; MB factor $\alpha\ N\ e^{-Ea/kT}$ where Ea is the separation of acceptor trap from valence band. In the present case, the faster recombination rate and hole capture eventually leads to slow response. Thus, from the rate equation it is suggested that, increasing the

total trap density D_{total} and MB factor and reducing W_{rec} and W_{cap} directly increases the photocurrent.

After attaining the saturation, the illumination is turned off and the obtained decay profile is due to Persistent Photoconductivity (PPC). By mono-exponential fitting, using the equation-

$$I = I_O + exp\frac{-t}{\tau} \quad (6)$$

The time constant attained is nearly 63 s for Eu^{3+}: CGO sample. PPC is associated with the deep level traps with a capture barrier. Initially recombination dominates and there is an abrupt fall in the photocurrent which slows down further due to thermal energy release. This fast decay is consistent with the μs lifetime from the TRPL studies. In the Na^+ codoped sample, there is almost a shoot in the photocurrent during steady illumination and no saturation current is observed. This significant rise in photocurrent is attributed to the Na^+ doping. It introduces deep acceptor levels in the energy band gap of CGO. With its small ionization potential, it easily releases electrons from the occupied acceptor level to the conduction band [39]. Hence, we get enhanced photoconductivity. Another observation is the reduction in PPC to a value of 58 s. This is because the Na^+ acceptor level has no effective barrier to trapping and it promotes the direct recombination process. This is also the reason why we get enhancement in the emission intensity of Na^+ co-doped sample.

In summary, likewise the intrinsic behavior of Ga_2O_3, this material also shows the property of fluorescence and photoconductivity, which is not very usual with other wide band gap materials. However, the photoconductivity is not up to the mark for pragmatic aspect (slow response time despite the significant photocurrent of μA) if one wants to utilize this property of the material for solar blind UV detector/converter application. However, on the other hand, the UV-excited efficient light emission (in red colour) by this material is accompanied by reasonably

good transmittance and no excitation channel in the whole visible and near-UV spectrum shows the suitability of the material for inorganic UV-to-visible converters. Such optical materials can be coupled to silicon-based commercial detectors for the imaging of UV events in wide areas ranging from invisible flame sensing to UV astronomy, etc.

Conclusion

A wide band gap material, $CaGa_2O_4$, co-doped with Eu^{3+} and Na^+ has been synthesized for nearly monophase formation. Optical properties show superiority over photoconductivity for UV sensing application. Host itself gives UV, blue and red emission driven by defects induced intraband transitions under UV excitation. Co-doping of Eu^{3+} and Na^+ widens broad band excitation features, by the involvement of host absorption band and associated trap levels, charge transfer state of Eu^{3+}, and also by exciting the characteristic f-f transitions of Eu^{3+} ions, in complete UV spectral region. Fairly good optical transparency, strong absorption in solar blind UV region, and intense emission in red region thereafter by this wide band gap material definitely demonstrate the feasibility of its application in wide areas ranging from invisible flame sensing to UV astronomy, etc

Acknowledgements

S. K. Singh thankfully acknowledges the financial support by Department of Science and Technology (DST), New Delhi, India in the form of INSPIRE Faculty Award [IFA12-PH-21]. M. Rai is thankful to UGC, New Delhi for junior research fellowship (RFSMS). K. Mishra is thankful to CSIR, New Delhi for senior research fellowship (SRF). Authors are thankful to Dr. A. K. Singh (Department of Physics, BHU) for fruitful discussion.

References

1. G. Chen, F. Abou-Galala, Z. Y. Xu and B. M. Sadler, *Opt. Express*, 2008,16, 15059.

2. Y. Taniyasu, M. Kasu, and T. Makimoto, *Nature*, 2006, 441, 325.

3. V. N. Sigaev, N. V. Golubev, E.S. Ignat'eva, A. Paleari and R. Lorenzi, *Nanoscale*, 2014, 6, 1763.

4. T. Tut, M. Gokkavas, A. Inal and E. Ozbay, *Appl. Phys. Lett.*, 2007, 90, 163506.

5. L. Sang, M. Liao and M. Sumiya, *Sensors,* 2013, 13, 10482.

6. X. Sheng, C. Yu, V. Malyarchuk, Y. H. Lee, S. Kim, T. Kim, L. Shen, C. Horng, J. Lutz, N. C. Giebink, J. Park and J. A. Rogers, *Adv. Optical Mater.*, 2014, 2, 314.

7. J. Debgupta, S. Mandal, H. Kalita, M. Aslam, A. Patra and V. Pillai, *RSC Adv.*, 2014, 4, 13788.

8. D. Gedamu, I. Paulowicz, S. Kaps, O. Lupan, S. Wille, G. Haidarschin, Y. K. Mishra and R. Adelung, *Adv. Mater.*, 2014, 26, 1541.

9. X. Xie, Z. Zhang, B. Li, S. Wang, M. Jiang, C. Shan, D. Zhao, H. Chen and D. Shen, *Opt. Exp.*, 2014, 22, 246.

10. M. Ieda, T. Ishimaru, S. Ono, N. Kawaguchi, K. Fukuda, T. Suyama, Y. Yokota, T. Yanagida and A. Yoshikawa, *Jpn. J. Appl. Phys.,* 2012, 51, 062202.

11. H. Chang, Z. Sun,' K.Y.F. Ho, X. Tao, F. Yan, W.M. Kwok and Z. Zheng, *Nanoscale*, 2011, 3, 258.

12. Y. N. Hou, Z. X. Mei, H. L. Liang, D. Q. Ye, C. Z. Gu, and X. L. Dua, *Appl. Phys. Lett.*, 2013, 102, 153510.

13. F. J. Aparicio, M. Holgado, A. Borras, I. B. Lezak, A. Griol, C. A. Barrios, R. Casquel, F. J. Sanza, H. Sohlström, M. Antelius, A. R. G. Elipe and A. Barranco, *Adv. Mater.,* 2011, *23*, 761.

14. X. Li, C. Zhu, X. Zhu, Z. Xu, X. Zhuang, X. Ji, F. Yan, *Appl. Phys. Lett.*, 2013, 103, 171110.

15. M. Razeghi and A. Rogalski, *J. Appl. Phys.,* 1996, *79*, 7433.

16. A. Balducci , M. Marinelli , E. Milani , M. E. Morgada , A. Tucciarone , G. Verona-Rinati , M. Angelone and M. Pillon , *Appl. Phys. Lett.*, 2005 , *86* ,193509.

17. E. Fortunato, D. Ginley, H. Hosono and D. C. Paine, *MRS Bulletin*, 2007, 32, 242.

18. L. Binet and D. Gourier, *J. Phys. Chem Solids,* 1998, 59, 1241.

19. S. Z. Karazhanov and P. Ravindran, *J. Am. Ceram. Soc.*, 2010, 93, 3335.

20. F. Liu, W. Yan, Y. J. Chuang, Z. Zhen, J. Xie and Z. Pan, *Sci Rep.*, 2013, 3, 1554.

21. P. Feng, J. Y. Zhang, Q. Wan and T. H. Wang, *J. Appl. Phys.*, 2007, 102, 074309.

22. S. K. Singh, D. G. Lee, S. S. Yi, K. Jang, S. S. Dong and J. H. Jeong, *J. Appl. Phys.*, 2013,113, 173504.

23. W. Feng, X. Wang, J. Zhang, L. Wang, W. Zheng, P. Hu, W. Cao, B. Yang, J. Mater. Chem. C, 2014, 2, 3254.

24. R. D. Shannon, *Acta Cryst*., *1976*, *A32*, *751.*

25. J. Jeevaratnam and F. P. Glasser, *J. Am. Chem. Soc., 1961, 44, 563.*

26. F. P. Glasser and L. S. D. Glasser, *J. Am. Chem. Soc.,1963,* 46, 377.

27. H. L. Zheng, Z. C. Zhang, J. G. Zhou ,S. S. Yang and J. Zhao, *Appl Phys A*, 2012, 108, 465.

28. D. L. Wood and J. Tauc, *Phys. Rev. B*, 1972, 5, 3144.

29. C. S. Vanithakumari and K. K. Nanda, *Adv. Mater.*, 2009, 21, 3581.

30. X. T. Zhou, F. Heigl, J. Y. P. Ko, M. W. Murphy, J. G. Zhou, T. Regier, R. I. R. Blyth and T. K. Sham, *Phys. Rev. B*, 2007, 75, 125303.

31. G. Blasse, and A. Bril, *J. Phys. Chem. Solids*, 1970, 31, 707.

32. F. A. Kröger and H. J. Vink, Solid State Physics, 1956, 3, 307.

33. S. K. Pantelides, *Rev. Mod. Phys.*, 1978, 50, 797.

34. A. K. Parchur, R. S. Ningthoujam, *RSC Adv.*, 2012, 2, 10859.

35. J. F. Weisz and E. A. Andrada e Silva, *Phys. Rev. B*, 1992-I, 45, 11042.

36. M. Johnson, S. V. Baryshev, E. Thimsen, M. Manno, X. Zhang, I. V. Veryovkin, C. Leighton and E. S. Aydil, *Energy Environ. Sci.*, 2014, DOI: 10.1039/c3ee44130j.

37. A. K. Parchur, A. I. Prasad, S. B. Rai, R. Tewari, R. K. Sahu, G. S. Okram, R. A. Singh, R. S. Ningthoujam, *AIP Advances*, 2012, 2, 032119.

38. T. E. Murphy, K. Moazzami, J. D. Phillips, *J. Electron. Mater.*, 2006, 35, 543.

39. E. Bonetti, L. D. Bianco, L. Pasquini and G. Matteucci, *J. Appl. Phys.*, 2001, 90, 4152.

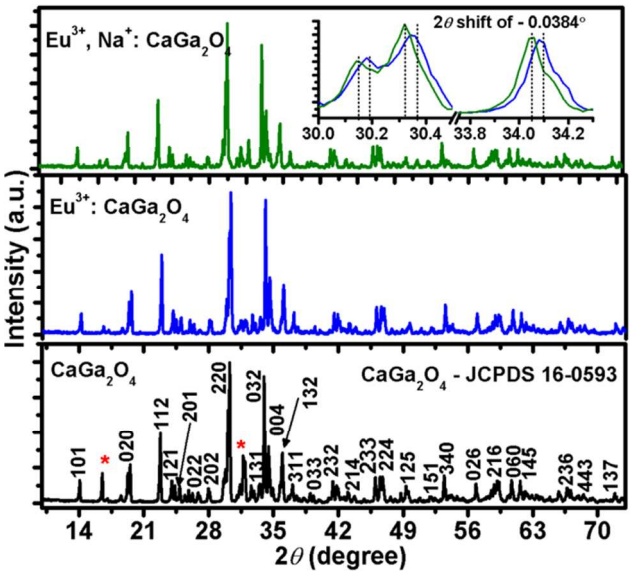

Fig. 1 X-ray diffraction patterns of $CaGa_2O_4$, Eu^{3+}(1 mol %) doped $CaGa_2O_4$ and Na^+(4 mol %), Eu^{3+}(1 mol %) co-doped $CaGa_2O_4$. Inset shows the peak shift due to Na^+ co-doping

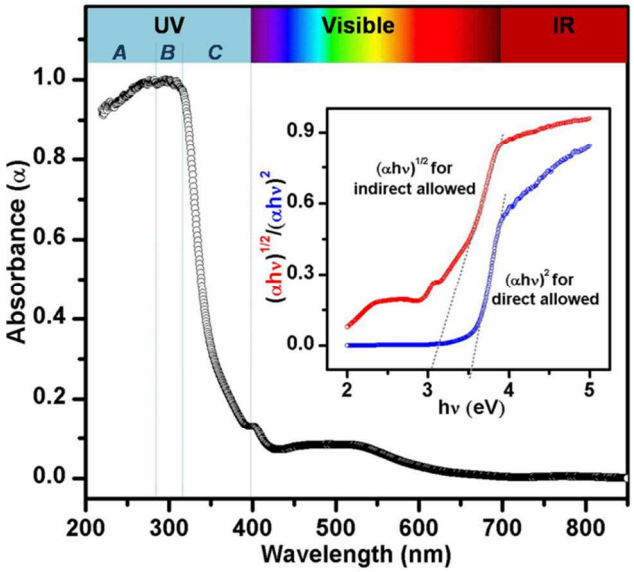

Fig. 2 UV-visible absorption spectrum of $CaGa_2O_4$ showing a strong absorption in Solar blind UV region. Inset shows the plot of $(\alpha h\nu)^2$ and $(\alpha h\nu)^{1/2}$ vs. photon energy ($h\nu$) for direct and indirect band gap measurement, respectively.

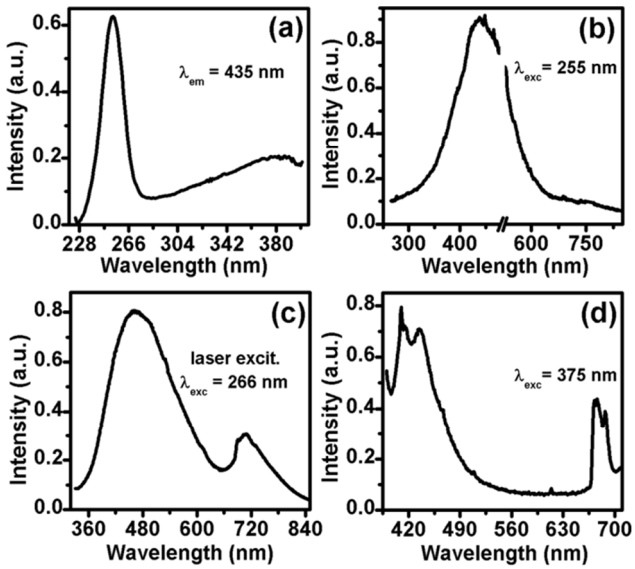

Fig. 3 Photoluminescence measurement of pure $CaGa_2O_4$ **(a)** excitation monitored for λ_{em}= 435 nm; **(b)** emission monitored at λ_{exc}= 255 nm; **(c)** emission under 266 nm laser excitation, and **(d)** emission monitored at λ_{exc}= 375 nm.

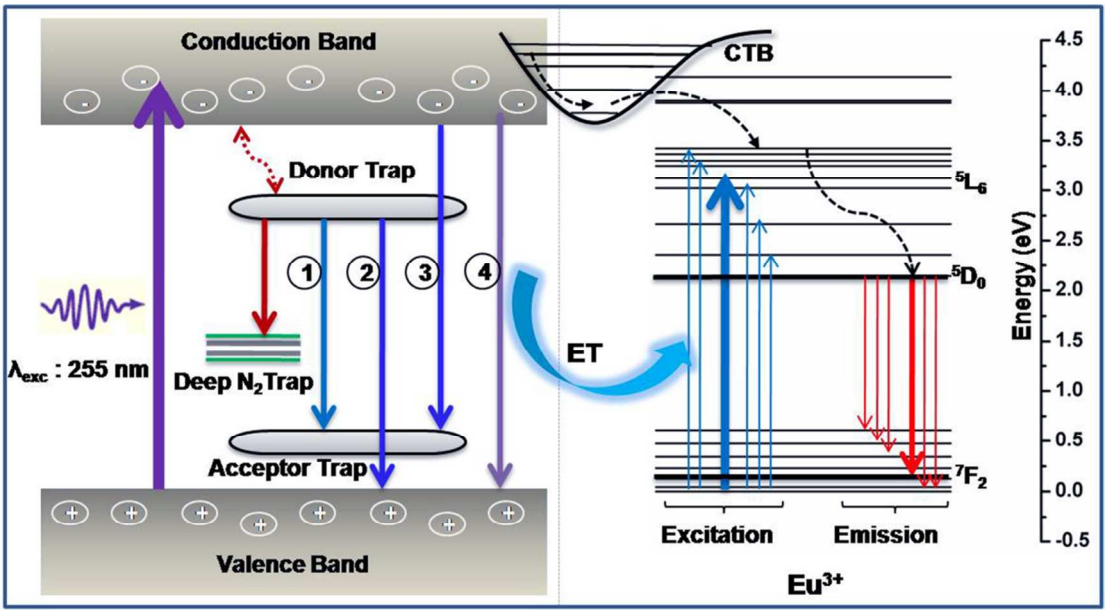

Fig. 4 Schematic representation of the energy bands/level and transitions involved in the emission of the $CaGa_2O_4$. Four different types of transitions 1-to-4, namely donar trap to acceptor trap, donar trap to valence band, conduction band to acceptor trap, conduction band to valence band, respectively, are observed mainly in UV-blue region. Deep nitrogen trap gives the emission in NIR region. The excitation energy of the host is transferred to the activator Eu^{3+} ions via charge transfer band (CTB) and energy transfer (ET) processes, and different electronic transitions of Eu^{3+} ($^5D_0 \rightarrow {}^7F_j$) in visible region is observed.

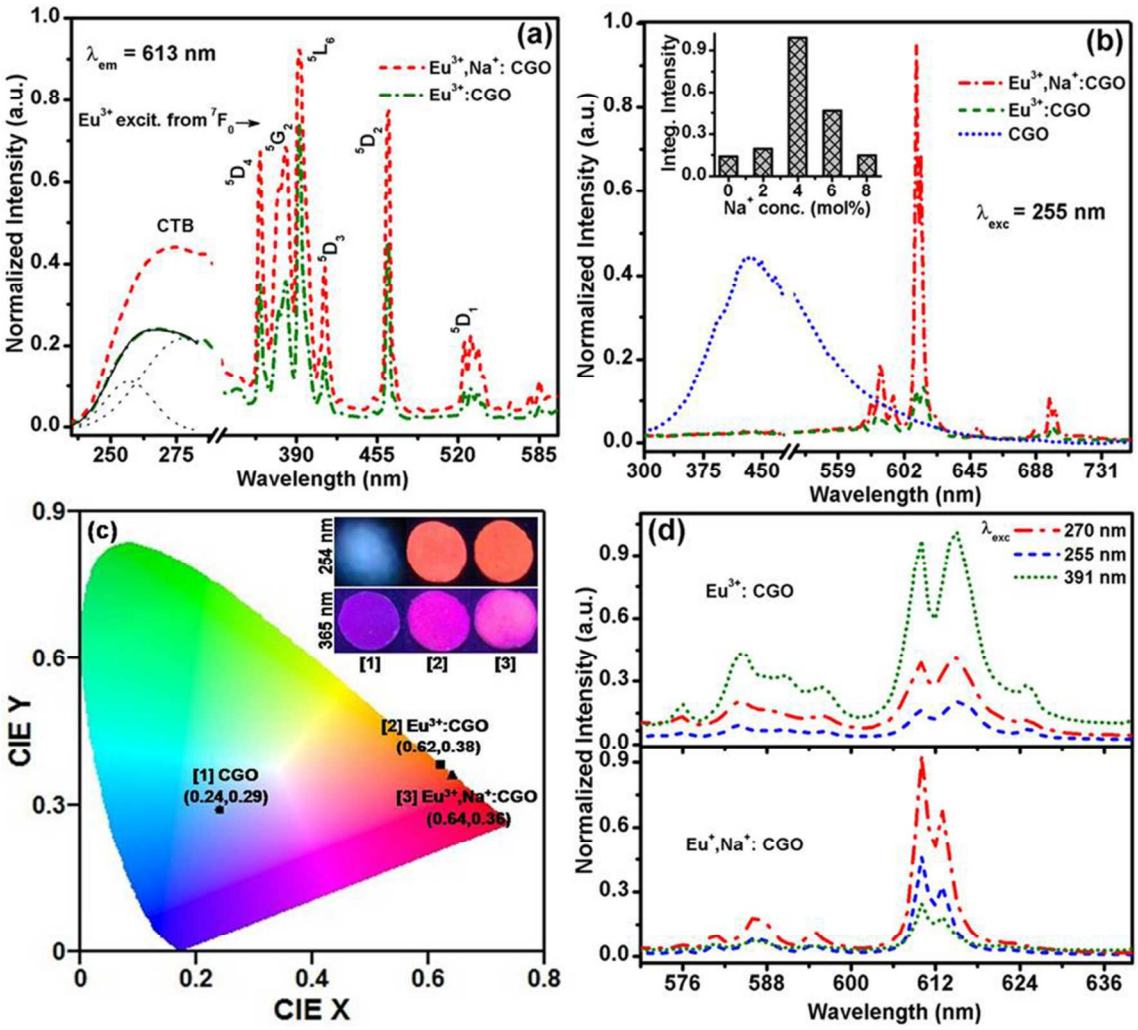

Fig. 5 Fluorescence measurement of Na^+ undoped/codoped Eu^{3+}:CGO **(a)** PLE monitored for λ_{em}=613 nm, **(b)** PL under 255 nm excitation, **(c)** CIE coordinate and digital photograph of the emission from different samples, **(d)** variation in the emission intensity of Eu^{3+} with a variation in the excitation wavelength.

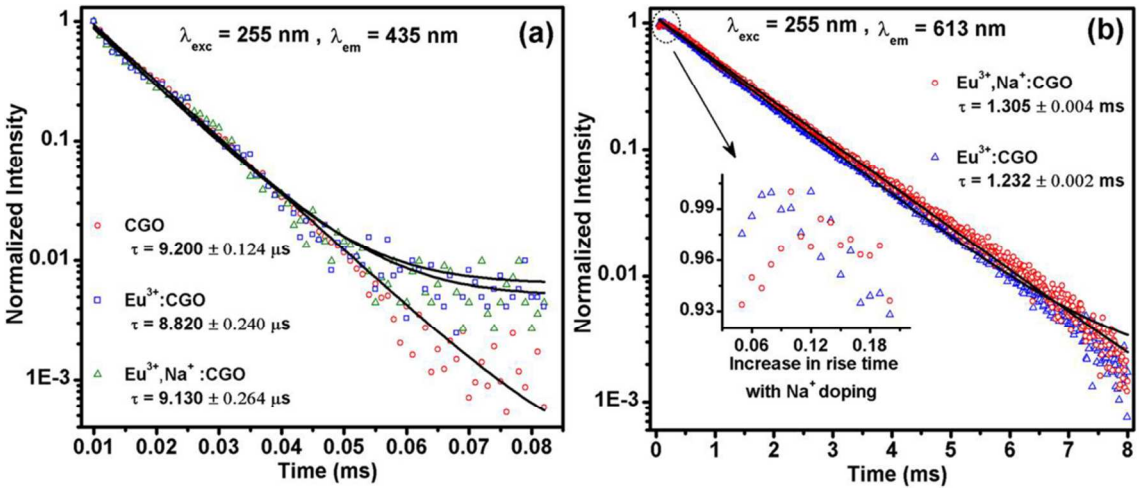

Fig. 6 Time domain fluorescence measurement under 255 nm excitation wavelength **(a)** host emission at 435 nm excitation, **(b)** Eu^{3+} emission at 613 nm ($^5D_0 \rightarrow {}^7F_2$)

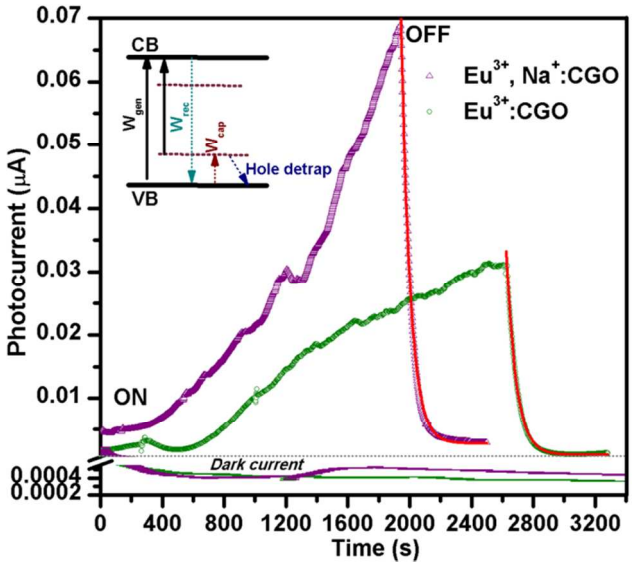

Fig. 7 Time resolved photoconductivity measurement of Eu^{3+}:$CaGa_2O_4$ and Eu^{3+}, Na^{+}: $CaGa_2O_4$

Table of contents

Schematic representation of energy bands/defect states, energy transfer and emission in Na^{+}, Eu^{3+}:$CaGa_2O_4$ usable for solar blind UV converter application.